JGR Planets

RESEARCH ARTICLE
10.1029/2019JE006255

Morphometric Characterization of Longitudinal Striae on Martian Landslides and Impact Ejecta Blankets and Implications for the Formation Mechanism

Alexa Pietrek[1], Stefan Hergarten[1], and Thomas Kenkmann[1]

[1]Institut für Geo- und Umweltnaturwissenschaften, Albert-Ludwigs-Universität Freiburg, Freiburg im Breisgau, Germany

Key Points:
- Longitudinal striae are scale-invariant and can be characterized using power spectral parameters that quantify relief and roughness
- Striae on both types of deposits share common characteristics that indicate a common formation mechanism
- We propose a formation mechanism that facilitates phase locking in the spectral domain

Correspondence to:
A. Pietrek,
alexa.pietrek@geologie.uni-freiburg.de

Citation:
Pietrek, A., Hergarten, S., & Kenkmann, T. (2020). Morphometric characterization of longitudinal striae on Martian landslides and impact ejecta blankets and implications for the formation mechanism. *Journal of Geophysical Research: Planets*, *125*, e2019JE006255. https://doi.org/10.1029/2019JE006255

Received 29 OCT 2019
Accepted 5 JAN 2020
Accepted article online 23 JAN 2020

Author Contributions
Conceptualization: Alexa Pietrek, Stefan Hergarten, Thomas Kenkmann
Methodology: Alexa Pietrek, Stefan Hergarten
Writing - Original Draft: Alexa Pietrek
Formal Analysis: Alexa Pietrek
Investigation: Alexa Pietrek
Supervision: Stefan Hergarten, Thomas Kenkmann
Visualization: Alexa Pietrek
Writing - review & editing: Alexa Pietrek, Stefan Hergarten, Thomas Kenkmann

Abstract Longitudinal striae are a shared characteristic of long run-out landslides and layered ejecta crater deposits. They appear to be a fundamental feature of disintegrated mass flows, but their formation and the required conditions are poorly understood. We evaluated their similarity using spectral analysis and assessed the possibility of a common formation mechanism. The topography of striae is scale-invariant in the form of a power law relationship of the power spectrum and the derived spectral exponent and amplitude factor, which are a measure for roughness, show similar correlations on both types of deposit. There is no correlation to geologic substrate units, latitude, or age. Parameter values are isotropic in horizontal direction for ejecta deposits and show a weak anisotropy for landslide deposits. Spectral parameter values of substrate topography match well with the values of the superposed deposit, which indicates that roughness is transferred from substrate to deposit surface during emplacement. Testing different geometric models, we find that a simple superposition of topography with a semideterministic, anisotropic pattern does not reproduce the patterns of our data. We find that phase locking of a surface with scale-invariant properties creates striae with fractal properties close to our natural data sets as well as recreating other morphological features that can form alongside striae. Although the transferal of substrate roughness cannot be fully conciliated with conventional flow models, we find that a model that combines advection with lateral diffusion accounts for the unidirectional preservation of phase information and is also consistent with the scale-invariance of striae.

Plain Language Summary Longitudinal striae are a prominent surface feature of many types of mass movements, for example, long run-out landslides on Mars and Earth and layered ejecta crater deposits. It is unclear how they form or whether they form by the same process on the different types of deposits. Using high-resolution remote-sensing data of pristine Martian landslides and layered ejecta craters, we find that the similar appearance of striae can be confirmed by shared morphometric properties. Fourier methods reveal a scale-invariant topography where the roughness of longitudinal and perpendicular profiles is surprisingly similar. It is even similar to the roughness of the topography outside the striated regions, so that it may be inherited from the underlying substrate. This weak anisotropy in roughness cannot be responsible for the distinct pattern of striae. The latter is probably related to the phases of the Fourier components rather than to the amplitudes that are responsible for the roughness. These characteristics include scale-invariance, weakly anisotropic fractal properties and a roughness that appears to be transferred from the substrate. Testing of formation models shows that a formation process that conserves phase information of topography is most consistent with our data. We suggest that a flow process that combines advection with lateral diffusion of topography can enable phase locking and is also consistent with the fractal properties of striae.

1. Introduction

Longitudinal striae (also denoted as "striations" or longitudinal ridges and grooves) are a distinct surface feature of mass movement deposits that can be observed in different environments and even on different planetary bodies. Terrestrial examples include rock avalanches emplaced on a glacial substrate such as Blackhawk (Johnson, 1978; Shaller, 1991) or Sherman landslide (McSaveney, 1987; Shreve, 1966) as well as volcanic pyroclastic flows and debris avalanches (Belousov et al., 1999; Naranjo & Francis, 1987; Valderrama et al., 2016). On Mars, those features are found on layered ejecta deposits of impact craters (Barlow et al.,

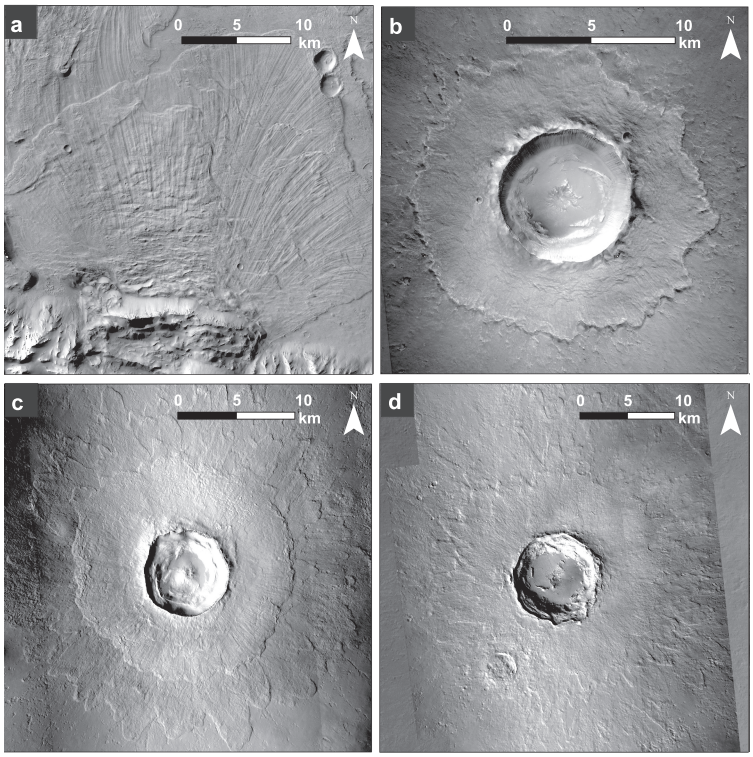

Figure 1. Examples of the four deposit types considered in this study. (a) Landslide deposits are structured into a proximal zone of chaotic and unstructured hummocky material and a large fan-shaped deposit that often develops distinct striations (Coprates landslide; data: CTX). (b) SLE craters have one continuous layer of ejecta deposits that often terminates in a thickened distal rampart (Naar crater; data: CTX image G19_025691_2031_XN_23N042W). (c) DLE craters are characterized by two clearly separable continuous layers. The inner layer has a circular perimeter and is characterized by a thickened rampart at the outer edge, while the outer layer consists of multiple lobes (Steinheim crater; data: CTX). (d) MLE craters have multiple lobes of ejecta that cannot be clearly grouped into separate layers (Domoni crater; data: CTX, HRSC).

2000) and long run-out landslides (Lucchitta, 1979; Quantin et al., 2004). The formation of striae is studied separately within the different fields and is still poorly understood. Recently, several studies noted similarities of morphological features between striations on landslide and impact ejecta deposits. They put forth the hypothesis that striations on ejecta deposits are an indicator for an emplacement mechanism that is similar to that of landslides (Weiss & Head, 2013, 2014; Wulf & Kenkmann, 2015). These studies were based on a qualitative comparison of the morphology of striations alone and did not include a quantitative evaluation. In this paper we focus on the development of a mathematical model and morphometric classification scheme that describes the statistical properties of striations and allows for a quantitative comparison between different deposits. Based on the analysis of topographic profiles of 23 Martian landslide and layered ejecta crater DEM (Digital Elevation Model) data sets, we assess the similarity of striation patterns on the different deposit types and the plausibility of a common formation mechanism.

2. Deposit Morphology and Classification

Martian impact craters show a wide spectrum of appearances and are usually classified by their ejecta morphology. All impact craters investigated in this study fall into the category of layered ejecta craters. Layered ejecta craters are surrounded by one or more layers of continuous ejecta. They are often attributed to have a "fluidized" appearance and unusual long run-out compared to impact craters with radial ejecta patterns as found on Moon and Mercury. In agreement with the standardized nomenclature of Barlow et al. (2000), we subdivide our craters into the three main classes: single-layered ejecta (SLE), double-layered ejecta (DLE), and multilayered ejecta (MLE) craters, depending on the number of continuous ejecta layers surrounding the crater (Figures 1b–1d). To date, two global Martian crater databases use this classification scheme (Barlow et al., 2000; Robbins & Hynek, 2012) and were referred to in our classification. We found that often

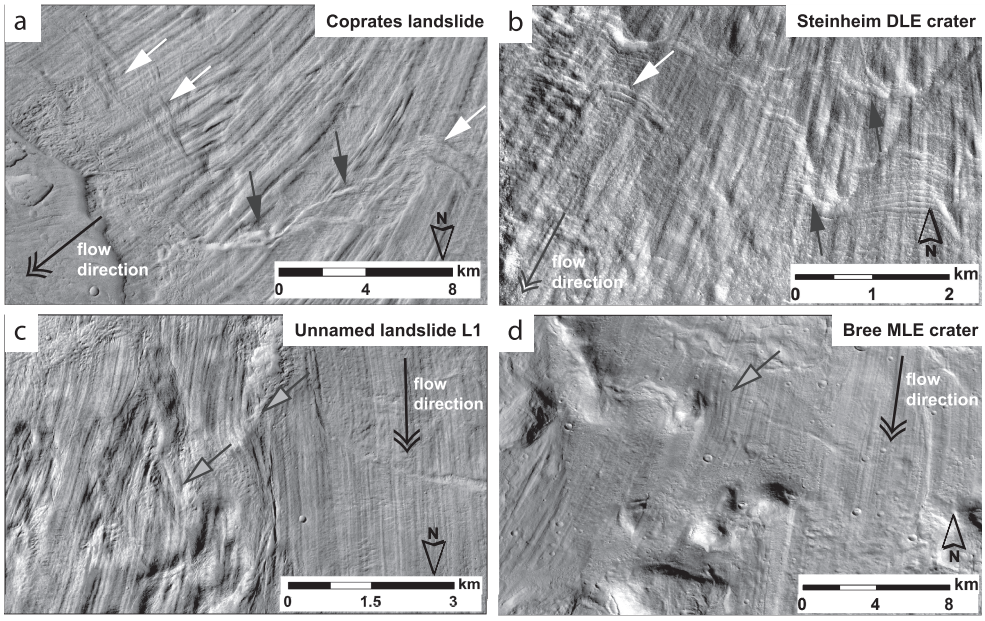

Figure 2. Examples for striae on long run-out landslides (a, c) and ejecta deposits (b, d). Common morphological characteristics are perpendicular graben (white arrows), internal flow lobes (black arrows), and deflection and bending of striae around obstacles (black-rimmed gray arrows). (a) Coprates landslide (ID L3). (b) Steinheim DLE crater (ID DL1, data: HiRISE image PSP_009160_2350, CTX image P17_007802_2349_XN_54N169W). (c) Unnamed landslide in Ganges Chasma (ID L1). (d) Bree MLE crater (ID ML2, data: CTX image B19_017193_2040_XN_24N237W).

there is a disagreement on the classification of DLE and MLE craters. This is partly owed to the relatively low pixel scale used in those studies (~100–300 m/px, respectively) and the more general problem that those types appear to be morphological end members, where many craters have morphologies that fall in the transitional area between. We therefore decided to use the term DLE crater if the following criteria are met: The inner ejecta facies is circular to moderately lobate (Figure 1c). It can be characterized by a thinner "moat" area in approximately the middle distance to the crater rim and terminates in a thickened rampart. In contrast, the outer facies is often composed of multiple thin lobes with a longer run-out. Striations are usually found mainly on the inner ejecta facies, but sometimes similar curvilinear structures may also appear on the outer ejecta facies (e.g., the outer facies of Bacolor crater or localized on small ramparts of the outer ejecta facies of Steinheim crater). On the inner layer, striations start to form in close proximity to the crater rim and continuously extend toward the rampart (Wulf & Kenkmann, 2015). In this study, we only consider striations found on the inner ejecta layer. The MLE craters in this study lack a clearly defined inner ejecta facies and consist of multiple overlapping lobes (Figure 1d). Striations usually start to form in the proximal region near the crater rim and continuously extend to varying distances around the crater perimeter. The landslides used in this study are mainly located in the large canyon system Valles Marineris, except for one landslide situated in Blunck crater that is also located in the southern hemisphere. Quantin et al. (2004) classified the Valles Marineris landslides as "structured deposits with debris aprons" (Figure 1a). Their proximal region near the landslide consists of blocks rotated along circular normal faults, followed by unstructured hummocky material. The larger part of the deposits consists of one to several overlapping debris aprons with a long run-out. The debris aprons have an even thickness that decreases slowly with distance. Ramparts at the distal edge, if present, are usually not well pronounced. This type of landslide typically has distinct striations that start to form in the proximal region shortly after the hummocky material and usually continue to the outer edge of the deposit.

3. Morphology of Striations

Striae are an apparently regular and distinct pattern of longitudinal ridges and grooves that shape large parts of the surfaces of landslide deposits and layered ejecta blankets on Mars (Figure 2 and Table 1). They are generally interpreted as markers for flow direction as they follow the deflection of landslide material along topography (Mazzanti et al., 2016).

Table 1
List of Data Sets

Deposit type	ID[a]	Area marked by striae/ deposit area (km^2)	Extent of striae[b]/ deposit run-out[c](km) (km)	Location[d]	Pixel scale of image data (m/px)	Number of profiles l/p/t/o[e]	Geologic unit[f]	Age (Ma)
Landslide	L1	1,390/2,335[g]	34 / 48.1	8.6°S 44.5°W	5.1	18/37/14/—	Htf	50[g]
	L2	275/320[g]	24 / 32.5[g]	7.6°S 44.2°W	5.1	9/49/14/—	Htf	700[g]
	L3 (Coprates)	1,820/1,930[g]	41 / 60.7[g]	11.8°S 67.8°W	5.1	27/192/14/—	Ht	400[g]
	L4 (Ophir West)	944/1,928[g]	54 / 60.7[g]	11.1°S 68.3°W	5.1	16/46/14/—	Ht	150[g]
	L5 (Ophir East)	45/50[g]	15 / 21.5	11.1°S 67.9°W	5.1	6/10/14/—	Ht	500[g]
	L6 (Melas)	1,420/1,670	38 / 62.7[g]	8.9°S 71.8°W	6.1	24/77/25/—	Ht	1500[g]
	L7 (Ius East)	>824/1,141[g]	37.5/59.3	8.1°S 77.6°W	5.7	11/58/14/—	Ht	1000[g]
	L8 (Baetis)	>1,580/3,416[g]	>33 / 66.3[g]	3.8°S 71.7°W	0.6	13/21/—/—	Htf	100[g]
	L9	271/445	18.3/24.8	27.5°S 37.0°W	4.7	8/15/7/—	Nh	
SLE crater	SL1 (Gratteri)	69/130	4/4.2	17.7°S 160.0°W	1.0	10/4/12/—	Nh	
	SL2 (Naar)	260/373	7.2/7.4	22.9°N 42.1°W	0.3	7/7/8/—	Htf	
	SL3	230/470	7.3/7.4	34.2°N 109.6°E	0.7	6/5/—/—	AHv	
	SL4	300/610	8.5/9	23.9°N 122.3°E	0.6	8/5/8/—	Ht	
	SL5 (Tomini)	97/152	5.0/5.3	16.3°N 125.6°E	0.9	9/8/—/—	Ht	
DLE crater	DL1 (Steinheim)	590/772	9.2/10	54.5°N 169.3°W	4.8	8/37/24/19	Ht	9.3 ± 0.74[h]
	DL2 (Bacolor)	1,590/1,930	20.9/22	33.0°N 118.6°E	5.5	20/81/9/26	AHv	161 ± 9.1[h]
	DL3	630/731	9.3/9.8	43.5°N 40.7°W	0.6	7/12/9/7	AHp	
	DL4 (Maricourt)	140/273	6.2/6.5	53.4°N 71.2°W	0.6	7/13/7/3	AHp	
MLE crater	ML1 (Arandas)	2,400/3,740	26.7/—	42.4°N 15.1°W	0.3	6/12/9/—	AHp	542 ± 42[i]
	ML2 (Bree)	1,900/3,100	21.4/—	37.6°N 149.6°E	0.8	7/14/9/9	AHp	
	ML3	370/410	7.4/—	45.4°S 25.7°E	0.5	17/16/—/25	Nh	
	ML4 (Domoni)	560/713	9.7/—	51.3°N 125.5°W	0.3	20/25/9/—	AHv	
	ML5 (Jaisalmer)	594/670	8.8/—	33.5°N 84.2°E	0.3	8/11/13/—	Ht	

[a]IDs are listed as used in text and figures, official names are in brackets. [b]Maximum extent of striae. [c]Run-out of landslides ($\approx L$) or striated ejecta facies. MLE craters are excluded since ejecta facies are not clearly separable. [d]Planetocentric coordinates, longitude increases in west and east direction with respect to the prime meridian. [e]Profiles used for spectral study. Profile types: l = longitudinal, p = perpendicular, t = terrain, o = outer layer. [f]Adopted and summarized from Tanaka et al. (2014). AHp: periglacially modified mantling material of Amazonian age or periglacially modified volcanic/volcanoclastic rocks or fluvial sediments of Hesperian age. AHv: Amazonian and Hesperian stacked flood basalts and lava flows. Ht: volcanic rocks and sediments of late Hesperian age, reworked by mass wasting. Htf: late Hesperian fluvial sediments or sediments modified by fluvial or aeolian processes. Nh: Noachian volcanic highland rocks, partially reworked by fluvial or aeolian processes or impact events. Martian periods: Pre-Noachian (4.5–4.1 Ga), Noachian (4.1–3.7 Ga), Hesperian (3.7–2.9 Ga), and Amazonian (2.9 Ga–present). [g]Adopted from Quantin et al. (2004). [h]Adopted from Wulf and Kenkmann (2015). [i]Adopted from Lagain et al. (2015)

Among their overall similar appearance, striae share some specific morphological features. The most common are perpendicular graben-like structures (Barnouin-Jha et al., 2005; Carr et al., 1977; Weiss & Head, 2013; Wulf & Kenkmann, 2015) and internal flow lobes (Figures 2a and 2b). The graben mostly appear in a cross-cutting relationship with striae, and individual ridges or grooves can often be traced across the graben structures. The graben are interpreted as extensional features (Shreve, 1966) and are expected to develop after the formation of striae (Wulf & Kenkmann, 2015). Internal flow lobes are locally developed tongue- or fan-shaped accumulations terminating with well-defined flow fronts or small ramparts at the distal edge. Their size is usually small compared to the total size of the respective deposit, and their formation is likely related to the occurrence of local flow instabilities at the surface of flows, which can lead to overflow of faster moving excess material. The interaction of flow lobes with striae is complex and the order of formation is not always clear. Generally, striations terminate at thick flow lobes, and striae in the underlying deposit is cut off sharply at the toe, but they cross over shallower lobes.

Another common characteristic is flow around obstacles or deflection by underlying topography that is indicated by the bending of striae in response to the changes in flow direction (Figures 2c and 2d). On landslide deposits, the spectrum of morphologies ranges between gradual bending of striae due to large-scale topographic changes (Figure 2a) to more complex disturbances of striae over rough ground or irregularly spaced obstacles. They often fan out in the distal part as a response to spreading of the deposit. In contrast, bending is less common on ejecta deposits (Figure 2d) and in most cases less pronounced. Striae on ejecta deposits generally form a straight radial pattern. This is most probably related to the radial trajectories and high velocity of excavated rock material, which then also results in a radial outward flow of ejecta deposits that can directly pass over obstacles (Boyce & Mouginis-Mark, 2006). Topographic depressions like preexisting impact craters are usually overrun in a straight line. However, large obstacles on the kilometer-scale or of a height significantly larger than the flow thickness of ejecta can cause deflection of striations at the edges and flow around the obstacles (Figure 2d). Similarly, some impact craters show local gradual bending of striations that might be due to underlying topographic changes.

Another characteristic of striae is that individual ridges or grooves can often be traced from the starting point of formation to the end of the deposit. On landslides it can moreover be observed that longitudinal ridges are often arranged in parallel groups that only terminate at the end of the deposit. Spreading of the deposit in the distal part causes the formation of new striations in the interstitials between those groups. On ejecta deposits, sets of parallel ridges usually do not exist. Since ejecta deposits are perpetually diverging in outward direction, new striations form evenly distributed in the interstitials between individual striations.

4. Formation Hypotheses of Longitudinal Striae

On landslides, the formation of striae is proposed to result from processes that occur during flow, for example, lateral spreading (Belousov et al., 1999) or lateral shear (Shreve, 1966). It has been noted that striations often form on rock slides deposited on a glacial substrate (McSaveney, 1987; Shreve, 1966), but similar features have also been described for deposits that presumably formed in a dry environment (Belousov et al., 1999; Naranjo & Francis, 1987; Valderrama et al., 2016). Laboratory experiments with granular material suggest that an erodible substrate (Dufresne & Davies, 2009), flow instabilities induced by differences in grain size (Pouliquen & Vallance, 1999; Valderrama et al., 2016) or vertical contrasts in flow density (Forterre & Pouliquen, 2001) can lead to the formation of longitudinal striae.

For layered ejecta deposits, the discussion of the formation of radial grooves and ridges is closely linked to the open question of the overall emplacement mechanism for the ejecta blankets itself. On dry, atmosphere-less planets like Moon or Mercury, ejecta blankets typically have a discontinuous radial texture that is attributed to ballistic ejection and sedimentation (Oberbeck, 1975). In contrast, layered Martian ejecta blankets have a much longer run-out and a fluidized appearance (Carr et al., 1977). It is a general consensus that the long run-out implies emplacement as a ground-hugging flow, but the role of substrate volatiles (Barlow, 2005; Barnouin-Jha et al., 2005; Boyce & Mouginis-Mark, 2006; Carr et al., 1977; Osinski, 2006; Weiss & Head, 2014; Wulf & Kenkmann, 2015) or interactions with the atmosphere (Komatsu et al., 2007; Schultz, 1992; Schultz & Gault, 1979) is still under debate. Accordingly, there are still two competing hypotheses for the formation of striae in ejecta deposits. They may be the result of erosion by atmospheric effects, for example, by atmospheric turbulence that accompanies crater formation (Schultz, 1992; Schultz & Gault, 1979) or scouring by a base surge that results from the collapse of an explosion column (Boyce & Mouginis-Mark, 2006). Alternatively, flow processes during the deposition of the ejecta facies may be responsible (Barnouin-Jha et al., 2005; Weiss & Head, 2014; Wulf & Kenkmann, 2015).

5. DEM Generation and Data

As data basis, we use CTX (Context Camera) and HiRISE (High Resolution Image Science Experiment) image data from the Mars Reconnaissance Orbiter Mission, which has the highest image resolution available (Malin et al., 2007; McEwen et al., 2007). Stereo image pairs were processed to DEMs with the software tools and standard routines of the AMES stereo pipeline (Moratto et al., 2010; NASA, 2017). CTX DEMs typically have a horizontal pixel scale of ~6 m/px and HiRISE DEMs have better pixel scales between ~0.3 and 1 m/px. There is no documentation on vertical accuracy, but the obtained DEMs are in good agreement to MOLA (Mars Orbiter Laser Altimeter) tracks, which have a vertical accuracy of ~1 m.

We investigated 9 landslides and 14 impact ejecta deposits (Table 1). Eight of the landslides are situated in the Valles Marineris and formed from partial collapse of the steep walls that bound the valley system. The landslide L9 formed farther south from collapse of the southern crater wall of the crater Blunck (~62 km diameter). The 14 impact craters are subdivided into SLE, DLE, or MLE craters depending on the morphology of the ejecta deposits. Most of them formed in the northern hemisphere at an intermediate latitude, with the exception of two that formed in the southern hemisphere at low to intermediate latitudes (data sets SL1, ML3). The studied deposits were chosen for pristine features. They show few signs of erosional or depositional modification in the striated area and predominantly appear to be of a young age that is indicated by a small number and size of superposed impact craters.

Four types of linear topographic tracks were extracted from the data sets. "Perpendicular" and "longitudinal" profiles were extracted from the striated deposit surfaces. Perpendicular profiles are oriented normal to striae, while longitudinal profiles are aligned along the ridge crests of striations. For comparison to substrate properties, topographic tracks from potential substrate units ("terrain" profiles) not related to the striation pattern were also evaluated for all deposit types. Based on the pristine appearance of the deposits, we assume that both the deposits and the immediate surrounding terrain were not strongly altered by erosional processes after formation. We therefore assume that the surface properties of the recent topography are a good approximation for the properties of the substrate at the time of deposition. For DLE and MLE craters, profiles from the outer ejecta facies ("outer layer" profiles) were extracted additionally since the striated inner facies supposedly was emplaced on top (Weiss & Head, 2014; Wulf & Kenkmann, 2015). We assume that the outer ejecta facies might be the actual substrate of the inner facies (instead of "terrain") for both crater types.

We used a regular spacing of 0.5 km between perpendicular profiles, whereas longitudinal tracks are irregularly placed along ridges. Both terrain and outer ejecta profiles are randomly oriented. Parts of the deposits that show clear signs of overprint or disturbance of striae were excluded. This includes coverage by sand, disturbance by older or younger impact craters, local irregularities in the topography of the substrate, but also overprint by internal flow lobes or other compressive structures that formed in the proximal regions of the deposits. We extracted the tracks with a sampling distance of $\delta x = 10$ m.

6. Spectral Analysis

Preliminary analysis of topographic profiles suggested that they might be self-affine fractals as already proposed for topography in a more general context (Fox & Hayes, 1985; Mandelbrot, 1967; Pelletier & Turcotte, 1996; Turcotte & Schubert, 1982). Fractal behavior of topography is not unusual, but somewhat surprising since striae on mass movement deposits are often perceived as regularly spaced features. This often leads to the expectation that there exists a characteristic frequency of ridges or a robust mean ridge width (Magnarini et al., 2019). However, self-affine scaling behavior implies that the profiles are scale-invariant and cannot be quantified by a characteristic length scale. In particular, a characteristic spacing between ridges or grooves cannot be defined in topographic profiles.

Fractional Brownian motion (fBm) has become a paradigm for self-affine fractals. It can be defined by the spectral properties of the considered signal (here the topographic profiles), that is, by the contributions of different frequencies or wavelengths to the total signal.

Spectral analysis has been successfully applied in several planetary studies (Aharonson et al., 2001; Balmino, 1993; Malamud & Turcotte, 2001; Nikora & Goring, 2004, 2006; Turcotte, 1987).

As an alternative to the spectral analysis, wavelet transforms have been widely applied during the last decades. As an advantage, wavelet transforms are also sensitive to spatial variations in the power spectrum (Little et al., 1993; Malamud & Turcotte, 2001), but in turn they lose sensitivity at long wavelengths. In contrast to the global studies considered by other authors, this study focuses on landslide and crater ejecta units that were formed in one event and cannot be subdivided into further geologic subunits. Since resolving spatial spectral inhomogeneities is not feasible for the relatively small scale of topographic data considered in this study and the coverage of a wide range of wavelengths is desired, we prefer the Fourier transform. This method gives equivalent results to wavelet analysis and allows to define parameters of the power law that have convenient physical units (introduced in the following) with regard to the length and height scale of the deposits.

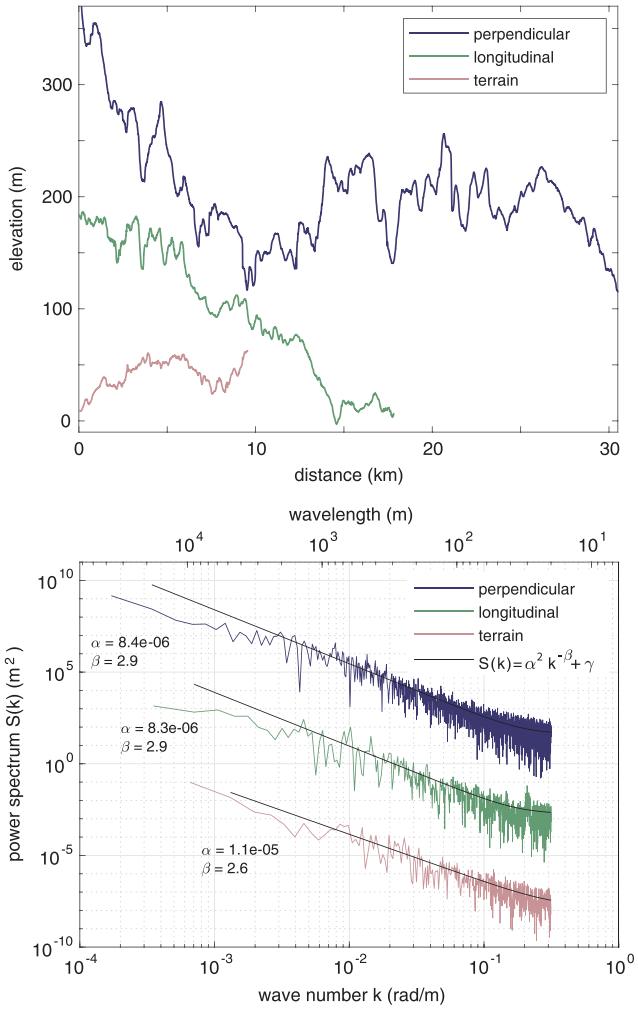

Figure 3. Examples of the three types of profiles (top) used in this study and corresponding power spectra (bottom; Coprates landslide). Power spectra are offset in vertical direction to avoid overlapping.

We decompose the topographic profiles $H(x)$ defined at the equally spaced points $x_1, \ldots, x_n$ into harmonic components using a discrete Fourier transform according to

$$H(x_l) = \sum_{j=-\frac{n}{2}+1}^{\frac{n}{2}} \phi_j e^{ik_j x_l} \tag{1}$$

where the wave numbers k_j are defined by

$$k_j = \frac{2\pi j}{n\delta x} \tag{2}$$

From the Fourier amplitudes ϕ_j we define the power spectrum at the wave number k_j as

$$S_j = \frac{2}{N^2}|\phi_j|^2 \qquad \text{for } 1 \le j < \frac{N}{2} \tag{3}$$

where the Fourier coefficients for $j \in \{0, \frac{N}{2}\}$ were omitted for simplicity.

The factor in front of the Fourier coefficients has been introduced for convenience in such a way that the power spectrum of a real harmonic function (a sine or cosine shaped profile) is $S_j = 1$ for the respective component for $1 \le j < \frac{n}{2}$.

The spectral representation of our profiles shows a power law dependence of S_j on the wave number k_j (Figure 3).

The real and imaginary parts of the Fourier coefficients of fBm are independent random numbers following a Gaussian distribution with expected values $\overline{\phi}_j = 0$ and variances defined by the power spectrum. As shown in Appendix A, the parameters of the power law relation can be obtained from a maximum likelihood estimate. This method has the advantage that it can be applied to individual profiles as well as to data sets consisting of multiple profiles. In order to take into account a potential additional uncorrelated variation in the topography at small scales due to the limited accuracy of the DEM, we extended the approach by white noise, so that the theoretical power spectrum reads

$$\overline{S_j} = ak_j^{-\beta} + \gamma \tag{4}$$

where a and β characterize the power spectrum of the fBm, while γ is the power spectrum of the white noise. White noise is visible at high wave numbers and separate accounting turns out to be useful for avoiding a bias in the exponents β toward lower values. However, we use γ only for avoiding this bias and do not analyze its dependency on any parameter (e.g., the type of the DEM) systematically. As it facilitates the interpretation, we rewrite equation (4) in the form

$$\overline{S_j} = \alpha^2 \left(\frac{k_j}{k_{\max}} \right)^{-\beta} + \gamma \tag{5}$$

with a new parameter α where $k_{\max} = \frac{\pi}{10\text{m}}$ is the maximum wave number defined by the sampling distance $\delta x = 10$ m of the profiles. This form has the advantage that α has the units of meters and can be seen as a linear measure of the vertical amplitude. It also increases the stability of the numerical scheme described in Appendix A.

As the discrete Fourier transform used in numerical data analyses assumes a periodic structure, it is in general susceptible to artifacts when applied to natural data. In particular, the periodic continuation may introduce a step in the profile that is also characterized by a power law spectrum (e.g., Hergarten ; 2002). In order to avoid this potential problem, we detrended each profile, although it has only a minor effect on the results for the profiles considered here.

7. Results of Fourier Analysis

The power law parameters α and β can be used to quantify the morphology of striations in terms of relief and roughness, respectively. Figure 3 shows three examples of topographic profiles and the respective power spectra. The parameter β is a measure for the relative contribution of wave number components; a high value means a higher contribution of long wavelengths and represents a smoother surface and vice versa.

The exponents β_s (single-profile estimations) for all data sets are shown in Figure 4. The variability in the exponents among the deposits appears to be larger than the variation within individual deposits. In order to investigate the variability among the deposits systematically, we assume that the scaling properties are constant for all profiles of a given type (longitudinal, perpendicular, etc.) within each deposit, that is, that each type of profile in each deposit can be characterized by a single value of β. The variation among individual profiles within a given deposit is then characterized by the amplitude factor α (and by the noise γ not investigated systematically in this study). Technically, a single exponent β and individual values of α and γ are determined by applying the Maximum Likelihood estimate described in Appendix **?** to all profiles simultaneously where the log-likelihood function is the sum of the individual log-likelihood functions. This method gives a more robust estimate of the overall scaling properties than the mean value of the β_s values obtained from individual profiles.

The results in Figure 4 show several interrelations.

1. The values for all data sets generally range between $\beta_s \approx 2$ and 3.5. On average, striated surfaces of DLE craters appear to be rougher ($\beta \approx 2.5$) than on landslides, SLE, or MLE craters ($\beta \approx 2.9$–3.1). Overall, there appears to be no characteristic value for striations in general or a certain type of deposit.
2. For each data set, β_s values for longitudinal and perpendicular profiles are in a similar range and there is no indicator for a strong anisotropy.
3. Under the premise that the direct substrate is represented by terrain profiles for landslides and SLE deposits and by the outer ejecta facies for DLE and MLE deposits, β_s values of substrate units agree well

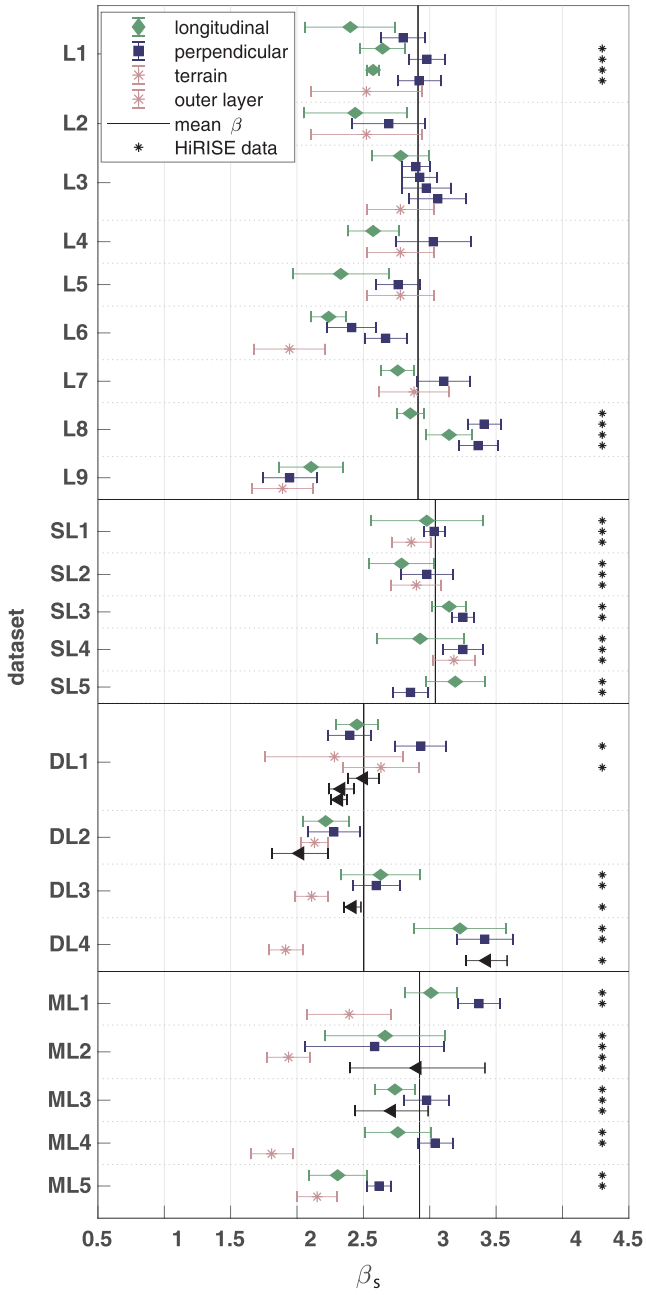

Figure 4. Comparison of the power law exponent β_s ordered by deposit. HIRISE data sets are marked with an asterisk on the right-hand side of the diagram (see Table 1 for actual pixel scales). Symbols indicate a representative β value for the whole set of profiles, σ is calculated from the individual values and indicated by whiskers. The β value indicated by a black line was estimated for all perpendicular and longitudinal profiles of one deposit type and can be interpreted as deposit average value. Note that terrain profiles are a proxy of the underlying substrate for landslide and SLE deposits. Outer layer profiles are extracted from a distal ejecta facies that only exists for DLE and MLE craters and that is supposedly overlain by the striated proximal deposits. The deposit data sets L1–L2 (L3–L5) use the same terrain profiles due to their close spatial proximity.

with β_s values of the deposits. In contrast, β_s values for terrain profiles of DLE and MLE deposits often have a significant negative offset that indicates that the deposit surface is rougher than the preimpact surface.

Several studies on fractal properties have been conducted for Mars, mostly on the base of global MOLA tracks that indiscriminately combine the spectral signal of different geologic units (Aharonson et al., 2001;

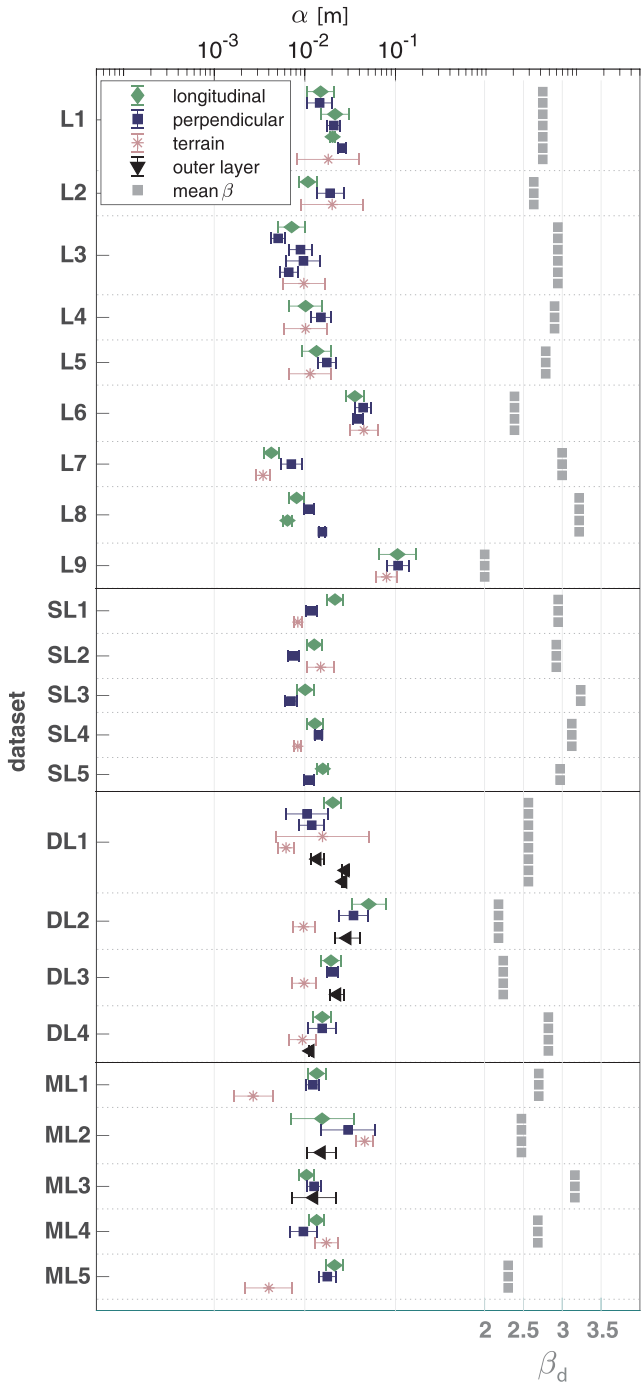

Figure 5. Comparison of the amplitude factor α ordered by deposit. The values were estimated with a single representative β_d value (gray squares) for each deposit to avoid bias in α values due to variations in β. Whiskers are the standard deviation to the mean representative α value indicated by symbols. The deposit data sets L1–L2 (L3–L5) use the same terrain profiles due to their close spatial proximity.

Balmino, 1993; Malamud & Turcotte, 2001; Nikora & Goring, 2006; Turcotte, 1987). Those studies predominantly found two scaling ranges with $\beta \approx 1.4$–2.4 for small wave numbers (≈10–300 km) and $\beta \approx 3.4$ for high wave numbers (≈0.7–7 km).

The topographic tracks in this study cover a smaller scale (≈0.2–80 km) and are associated with uniform geologic units. We found that β values vary greatly even for each deposit, but are on average $\beta \approx 2.9$ for

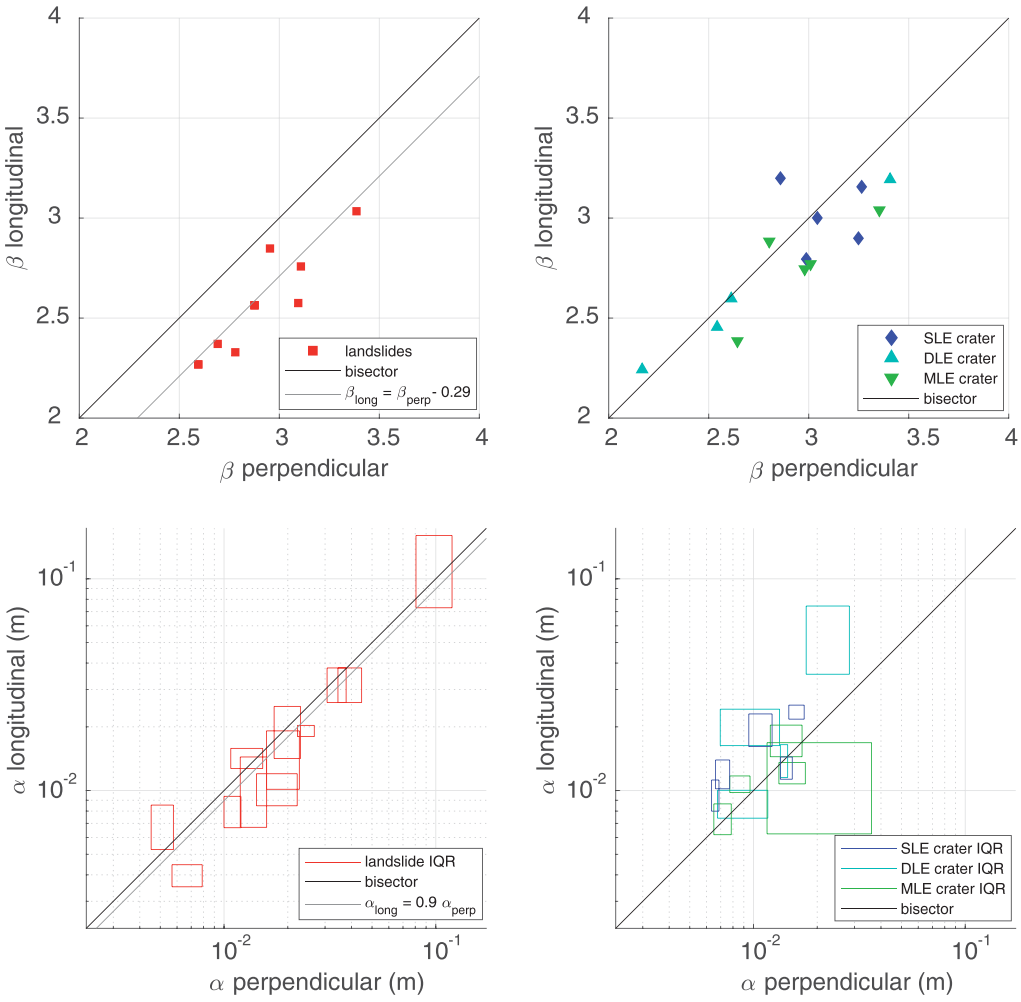

Figure 6. Comparison of parameter values β and α in longitudinal versus perpendicular direction for each deposit. Deposit types are separated into landslides (left diagrams) and layered ejecta craters (right diagrams). (upper row) Comparison of β values. Each data point is a pair of representative β values for longitudinal and perpendicular profiles of one deposit. The bisector marks an isotropic scaling relationship. (lower row) Comparison of α values. Each rectangle represents the Inter Quartile Range (IQR) of individual profile estimations. For the estimation of individual α values, a single representative β values (see Figure 5) was estimated for the combination of longitudinal and perpendicular profiles to avoid bias that otherwise arise from fluctuations in β.

landslide, SLE, and MLE deposits and $\beta \approx 2.5$ for DLE deposits, which is still in good agreement with the results on the high wave number end of the spectrum considered by other authors.

The amplitude factor α can be used to compare the overall relative height difference of ridges between data sets since a change of α in the power spectrum is equivalent to scaling the topographic signal in vertical direction. A direct comparison of α values is only reasonable for similar exponents β since the slope of the power law also influences the intersection point with the axis at the common wave number k_{max}.

To compensate the variability of α due to fluctuations of β_s within deposits, the joint likelihood approach of Appendix **?** was applied to both longitudinal and perpendicular profiles of each deposit to obtain a single β_d value. This value was used as a constant parameter for the calculation of α for the individual profiles. This allows the direct comparison of α in longitudinal versus perpendicular direction as it is shown in Figure 6 and a tentative comparison between deposits with similar β_d values in Figure 5. The results shown in Figure 5 reveal similar behaviors and correlations as the β_s values in Figure 4, most importantly the isotropy of values within each deposit and the similarity of values between deposits and their substrate.

Another aspect of fractal surfaces is the scaling relationship β in dependence on direction. For topography, it is generally assumed that surfaces are self-similar in the horizontal plane, that is, that surfaces scale isotrop-

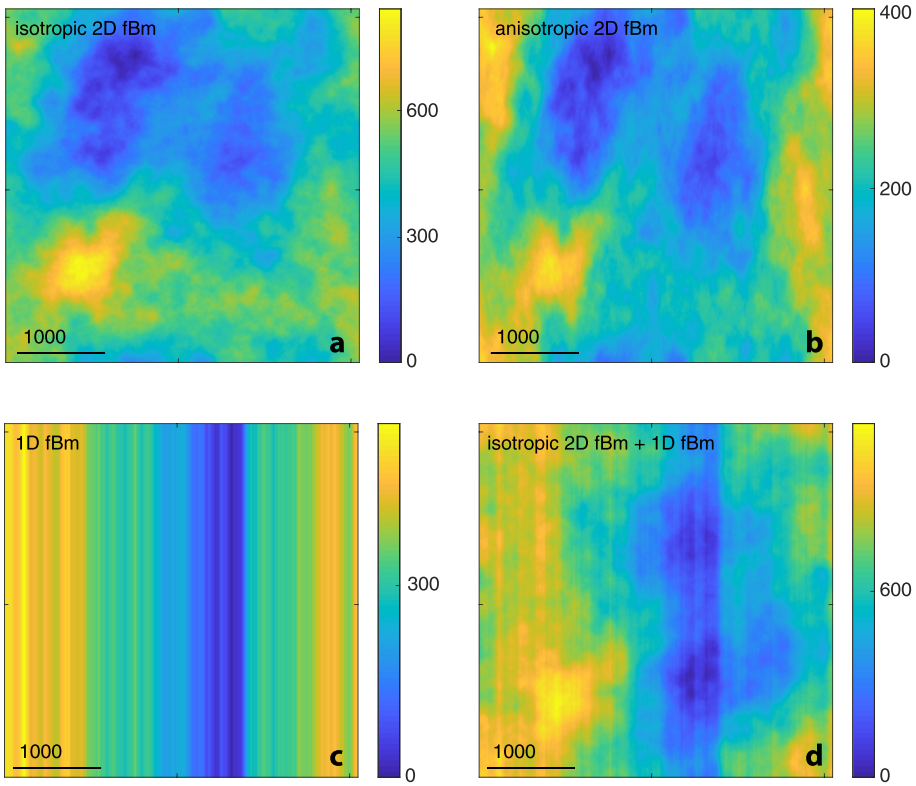

Figure 7. Comparison of different realizations of fBm. (a) Isotropic fBm with a spectral exponent $\beta = 2.7$. (b) Anisotropic fBm. The strength of anisotropy was chosen to match the anisotropy of α values observed in landslide data sets. Although the anisotropy is distinctive, no visual impression of actual striations is recreated. (c) Linear pattern that is 1-D fBm with an exponent of $\beta = 2.7$. (d) Superposition of the isotropic fBm with the linear pattern.

ically regardless of directions. The results show that the exponent β is nearly isotropic for crater deposits, but weakly anisotropic for landslide deposits (Figure 6). The difference in β values is a systematic decrease of β in longitudinal direction for all data sets and amounts to an average of $\Delta\beta = 0.29$. The scaling factor α has more convoluted results, but for landslides the values are shifted slightly to lower values in longitudinal direction. Apart from the correlation between substrate and deposit parameters, there appears to be no other systematic correlation of β and α to other deposit properties listed in Table 1, that is, not to the geologic units of the substrate.

In conclusion, striae on landslide and crater ejecta deposits are quite similar in their statistical properties and also show similar interrelations of power law parameters (e.g., the similarity to substrate properties or general similar range of values independent of direction). Although landslides show a weak anisotropy, we will demonstrate in the following that it is not responsible for the visual effect of an organized pattern of striations.

8. Geometric Models of Longitudinal Striae

Our results revealing almost isotropic statistical properties of striae are not consistent with the perception as strongly anisotropic patterns (see Figure 2). Examples of modeled isotropic fBm and anisotropic fBm are shown in Figures 7a and 7b. The parameters were adjusted to match the average differences in fractal properties between longitudinal and perpendicular profiles observed in our real data (see comparison of parameter results in Figure 8). While the anisotropy is visible in the pattern, there are no structures similar to the striations found in the natural topographies (cf. Figure 2 or Figures 9c and 9d). This leads to the conclusion that striations cannot be comprehended only by their power spectrum.

The finding that the fractal properties of striated surfaces are not only almost isotropic but are also close to those of the surrounding unstriated terrain suggests that the topography could be a superposition of the original terrain and a weak, but highly anisotropic pattern (representing a flow pattern) that is too small to

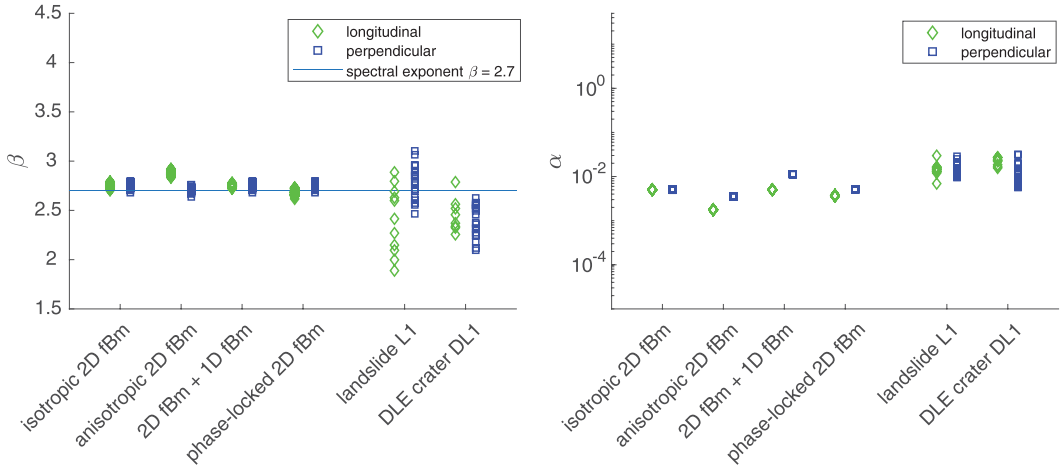

Figure 8. Comparison of spectral parameters for model fBms and real data sets. Values are derived from longitudinal and perpendicular tracks extracted from the model fBms created in Figures 7a, 7b, 7d, and 9b and from the data sets L1 and DL1 in Figures 9c and 9d. Although the values of real topographies show a larger spread due to natural irregularities, a phase-locked fBm most closely reproduces the patterns of the natural data sets.

modify the power spectrum significantly. Laboratory experiments of granular flow suggest that flow instabilities can lead to the formation of longitudinal striae (Forterre & Pouliquen, 2001; Pouliquen & Vallance, 1999) and a flow mechanism that allows "blanketing" of topography in the context of the formation of striations on landslides was suggested by DeBlasio (2011). Blanketing of topography by a mass flow deposit can be modeled phenomenlogically by superposing a pattern that varies only in one direction to an isotropic 2-D fBm representing the substrate. In order to leave the exponent β unaffected, we assume that the superposed topography is 1-D fBm (Figure 7c) with the same exponent (in the direction of its variation) as the underlying 2-D fBm (Figure 7a).

An example of such a superposed topography where we assumed that the amplitudes of both superposed patterns are the same is shown in Figure 7d. While this situation indeed yields a visual impression similar to real data sets (Figure 9), no clear striations are found if the amplitude of the superposed 1-D fBm is much smaller than the amplitude of the underlying 2-D fBm. We found a lower limit for the amplitude of the superposed 1-D fBm of about 80% of the amplitude of the 2-D fBm where striations become recognizable.

Since the superposed 1-D fBm is constant in longitudinal direction, the longitudinal amplitude factor α_l of the combined topography is the same as the amplitude factor of the isotropic underlying topography. As the two superposed topographies are statistically independent, the amplitude factor α_l and the perpendicular amplitude factor α_p of the combined surface are given by

$$\alpha_l = \alpha_s \tag{6}$$

$$\alpha_p = \sqrt{\alpha_s^2 + \alpha_{lp}^2} \tag{7}$$

where α_s is the amplitude factor of the underlying substrate and α_{lp} the amplitude factor of the superposed 1-D fBm. This leads to the relation

$$\frac{\alpha_p}{\alpha_l} = \sqrt{1 + \left(\frac{\alpha_{lp}}{\alpha_s}\right)^2} \tag{8}$$

So the limit $\frac{\alpha_{lp}}{\alpha_s} \gtrsim 0.8$ requires $\frac{\alpha_p}{\alpha_l} \gtrsim 1.3$.

Testing the $\frac{\alpha_p}{\alpha_l}$ ratio of our data we find that only 5 out of 23 data sets meet this condition. The overprint of a lineated flow pattern to a given topography is therefore not consistent with the majority of our data sets.

So neither a moderately anisotropic fBm nor the superposition of a striated surface pattern to an isotropic fBm reproduces our data. This finding suggests that the striation pattern relies on topographic information going beyond the power spectrum.

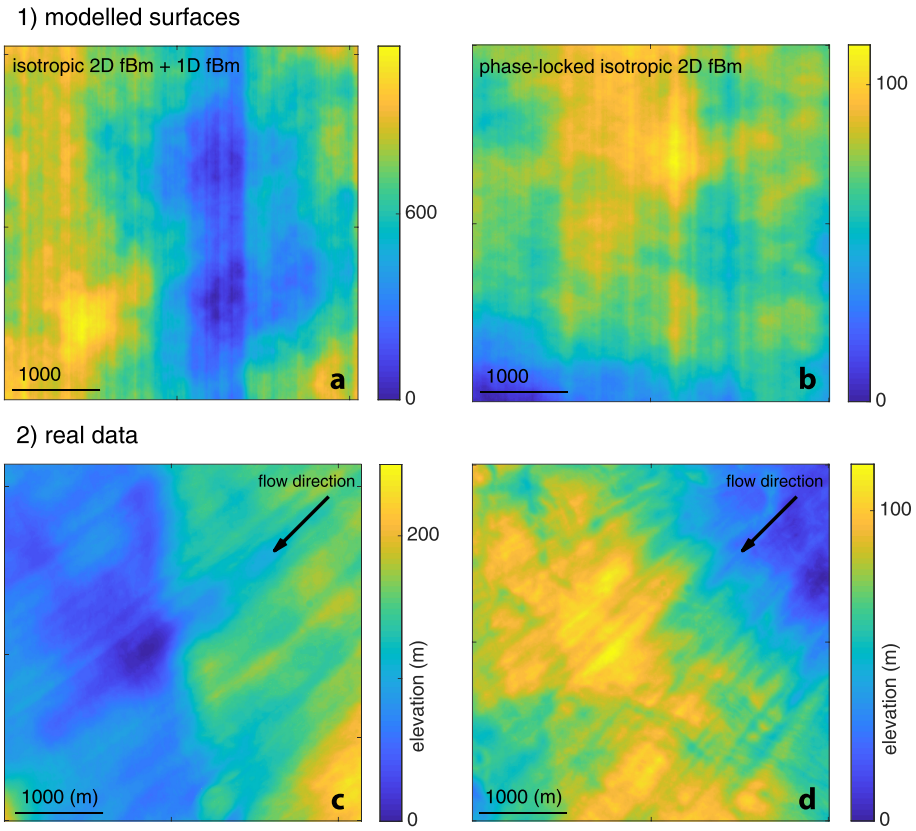

Figure 9. (1) Comparison of model fBms specified in the text with details of DEMs of real data sets. (a) 1-D fBm overprinted with isotropic fBm. (b) Unidirectional phase-locked fBm with statistically isotropic power law parameters. Note how phase locking creates a similar impression as real data sets and also recreates morphological features like perpendicular graben-like structures. (2) Details of DEMs used for evaluation. (c) Landslide L1. (d) Steinheim DLE crater (ID DL1).

9. Role of Phase Locking

As the coefficients in a Fourier decomposition are complex numbers, the power spectrum derived from the absolute values of these coefficients carry only half of the information contained in the topography. The rest can be expressed by the phases of the complex coefficients. As it was already shown by Hergarten (2002), fBm-type signals can be changed to completely regular signals and vice versa just by aligning the phases without changing the power spectrum.

It can be expected that changes in phases have even a stronger influence on the visual impression of a profile than changes in amplitudes. As phases of Fourier components of different topographic profiles cannot be related absolutely, we need the consideration of artificial topographies here, too. We have therefore generated fBm-type surfaces with artificially synchronized phases in one direction in order to find out whether synchronization of phases can generate striated patterns without affecting the power spectrum. For this purpose, a 2-D fBm pattern is first transformed to the frequency domain in x direction by a 1-D Fourier transform. Then the phases of the Fourier coefficients of the parallel profiles (belonging to different y values) are artificially synchronized, while leaving the absolute values unchanged. Finally, the pattern is transformed back to the spatial domain in x direction. Practically, the algorithm starts from Fourier coefficients consistent with 2-D fBm, transforms them in y direction to the frequency domain, synchronizes the phases, and ends with a 1-D Fourier transform in x direction.

The result is shown in Figure 9. Phase locking creates a similar pattern as the superposition of isotropic fBm and linear pattern and also compares well to DEM details of the real data sets. It is remarkable that graben-like structures very similar to those on real deposit surfaces are also reproduced. The results of the

power spectral analysis (Figure 6) also match well to the patterns described for real data, including the slight down shifts of α and β in longitudinal direction.

10. Implications for Potential Flow Mechanisms

The results of the geomorphic analysis presented in section 7 cannot provide a model for the flow process, but yields at least constraints on potential flow mechanisms. Among the geometric models considered in section 8, the data provide strong support for the model of synchronized phases.

The simplest fluid-dynamical model for flow in lateral direction is the shallow-water approximation where only horizontal flow is considered and acceleration is due to lateral pressure differences arising from the topography of the fluid surface. If friction is disregarded, this model leads to the well-known shallow-water waves. The simplest version including friction is considered in Appendix B. It is shown there that moderate friction preserves wave propagation, but with an amplitude decreasing through time. This means that the amplitudes of the Fourier coefficients decrease though time, and the phases also change. At a given threshold, however, propagation of waves ceases, so that the behavior turns into pure diffusion. This means that the amplitudes still decrease through time, while the phases remain constant.

The nonlinear behavior of viscous fluid layers has also been studied in the literature. More than 40 years ago, (Smith, 1973) investigated lateral spreading of viscous flow. While a strongly nonlinear dependence of the geometrical properties on time was found, the behavior is also diffusive in principle. In this sense, the model of synchronized phases tentatively points toward lateral flow normal to the low direction with a rather high friction.

While the model of synchronized phases even explains the slight anisotropy of the power spectrum, it cannot explain why the fractal properties of striated domains are close to those of the surrounding region. There seems to be no plausible process that directly takes over the amplitudes of the Fourier coefficients of an existing topography and synchronizes their phases. Instead, the existing topography should rather be some kind of source term in the equation of flow. For the diffusion equation, it was already shown by Aharonson et al. (2001) that white noise as a source term results in a self-affine topography with a spectral exponent $\beta = 2$ over long times. This result can be generalized to an arbitrary fBm-type source term. If this source term has spectral exponents β_{sp} concerning the spatial coordinates and β_t concerning time, the spectral exponent of snapshots of the topography will be $\beta = \beta_{\mathrm{sp}} + \beta_t + 2$. This implies that the spectral exponent of the resulting topography could indeed be controlled by the spectral exponent of the underlying topography. However, developing a physically reasonable flow model would go beyond the scope of this paper.

11. Conclusions

We found that the topography of striae is scale-invariant and cannot be distinguished by a characteristic width or height. Instead, they can be described in terms of roughness parameters that can be derived from their power law relationship in the spectral domain. We evaluated dependencies of the spectral exponent β, that is a measure for roughness, and the vertical scaling factor α, that is a measure for relief. It is common for all deposit types that

1. landslide and layered ejecta crater deposits show the same correlations (or lack thereof) for α and β values and can be considered morphometrically similar;
2. the values of β and α do not depend on the geologic substrate unit, latitude, or any dimensional property (e.g., deposit volume, area, and crater site);
3. there is no characteristic β value for any deposit type, although the average value for DLE craters ($\beta_{\mathrm{d}} \approx 2.5$) appears to be lower than the average value for SLE, MLE, and landslide deposits ($\beta_{\mathrm{d}} \approx 2.9$–$3.1$);
4. for landslides and SLE craters, there seems to be a correlation of β and α values between substrate (terrain) and deposit surfaces, as they fall into the same range;
5. for DLE and MLE ejecta crater deposits, β_{s} and α values fall into the same range as the values for the outer ejecta facies, while the values of the terrain often show a significant offset toward lower values. We interpret this as confirmation that the inner ejecta facies is emplaced over the outer facies and that the correlation between substrate and deposit is confirmed;

6. the former two items suggest that substrate topography is transferred to the deposit surface during deposition. We find that the simple phenomenological model of a superposition of topography and a lineated pattern (that is supposedly flow-generated) does not reproduce the anisotropy of β and α of our data;
7. we find that even the observed weak anisotropy in landslide data sets is not sufficient to fully describe or account for striations. Instead we find that unidirectional phase locking of a 2-D fBM reproduces striations. Since phase information is not included and has no influence on the power spectrum, it is consistent with the weak isotropy of β in our data sets. Interestingly, morphological details like graben structures that typically occur in nature together with striations are also reproduced, as well as the anisotropy in α values we observe in our data sets; and
8. although the overtaking of fractal properties from substrate to deposit surface is difficult to fully conciliate with conventional flow models, the hypothesis of phase locking is in favor of a process that is diffusion dominated in lateral direction.

We conclude that striae on landslide and layered ejecta crater deposits are indeed morphometrically very similar, as it was already proposed on a qualitative observation basis by other authors. Common morphometric properties are in favor of a common formation mechanism and we propose a flow process that enables phase locking to explain the formation of striations. Evaluation of common flow models suggest that high friction in direction of propagation can turn a wave equation into lateral diffusion, which preserves phases. The overtaking of substrate roughness cannot be fully conciliated, but we suggest that substrate topography could influence deposit properties if it acts as a source term in combination with a diffusion equation.

Appendix A: Application of the Maximum Likelihood Method to Fractional Brownian Motion

The ML method determines the most likely values of the adjustable parameters in such a way that the probability to obtain the observed data becomes maximal. The joint probability density corresponding to the values $S(k)_1, \ldots, S(k)_n$ is $\prod_{j=1}^{n} f(S(k)_j)$. Maximizing this expression is equivalent to maximizing its logarithm

$$L = \ln \prod_{i=1}^{n} f(S_j) \tag{A1}$$

$$= \sum_{j=1}^{n} \ln f(S_j). \tag{A2}$$

By assuming a Gaussian distribution for S_j equation (A2) can be written as

$$L = \sum_{j=1}^{n} -0.5 \left(\ln 2\pi + \ln \sigma_i^2 + \frac{S_j}{\sigma_j^2} \right). \tag{A3}$$

We then use the power law relationship from equation (5) for the variance σ_j^2 and can neglect the constant first logarithmic expression to obtain

$$L = -\frac{1}{2} \sum_{j=1}^{n} \ln \left(\alpha \left(\frac{k_j}{k_{\max}} \right)^{-\beta} + \gamma \right) + \frac{S_j}{\alpha \left(\frac{k_j}{k_{\max}} \right)^{-\beta} + \gamma}. \tag{A4}$$

This expression can be maximized numerically with respect to the parameters α, β, and γ.

Fractional Brownian Motion is characterized by Fourier components ϕ_j where both the real parts and the imaginary parts are independently Gaussian distributed with zero expected value and a variance σ_j^2 depending on the wave number. This variance is

$$\sigma_j^2 = \overline{Re(\phi_j)^2} = \overline{Im(\phi_j)^2} = \frac{1}{2} \overline{|\phi_j|^2} \tag{A5}$$

$$= \frac{N^2}{4} \bar{S}_j \tag{A6}$$

according to equation (3) since $|\phi_{-j}| = |\phi_j|$ for any real function H. Then the probability density for the real and imaginary parts of ϕ_j is

$$f(Re(\phi_j), Im(\phi_j)) = \frac{1}{2\pi\sigma_j^2} e^{-\frac{Re(\phi_j)^2 + Im(\phi_j)^2}{2\sigma_j^2}} \tag{A7}$$

$$= \frac{1}{2\pi\sigma_j^2} e^{-\frac{|\phi_j|^2}{2\sigma_j^2}} \tag{A8}$$

$$= \frac{N^2}{4\pi\bar{S}_j} e^{-\frac{S_j}{\bar{S}_j}} \tag{A9}$$

The resulting joint probability density of all independent Fourier coefficients is then given by the product $\prod_{j=0}^{\frac{n}{2}} f(Re(\phi_j), Im(\phi_j))$. Assuming that the expected power spectrum $\bar{S}_j$ depends on a set of parameters to be estimated, the respective logarithmic likelihood function is

$$L = \ln\left(\prod_{j=1}^{\frac{n}{2}} f(Re(\phi_j), Im(\phi_j))\right) \tag{A10}$$

$$= \sum_{j=1}^{\frac{n}{2}} \ln f(Re(\phi_j), Im(\phi_j)) \tag{A11}$$

$$= \sum_{j=1}^{\frac{n}{2}} \left(\ln\left(\frac{N^2}{4\pi\bar{S}_j}\right) - \frac{S_j}{\bar{S}_j}\right) \tag{A12}$$

$$= -\sum_{j=1}^{\frac{n}{2}} \left(\ln \bar{S}_j + \frac{S_j}{\bar{S}_j}\right) + \text{const} \tag{A13}$$

As the constant term can be neglected when maximizing the logarithmic likelihood function, inserting the modified power law function for $\bar{S}_j$ (equation (5)) directly leads to equation (A4).

If we consider scaling a real signal $H(x_l)$ by a real number $\hat{\alpha}$, the Fourier transform can be rewritten as

$$\phi_j = \hat{\alpha} \sum_{l=-\frac{n}{2}+1}^{\frac{n}{2}} H(x_l) e^{-ik_j x_l} \tag{A14}$$

Since

$$S_j = |\phi_j|^2 \approx \alpha^2 \left(\frac{k_j}{k_{\max}}\right)^{-\beta} + \gamma \tag{A15}$$

it follows that

$$\hat{\alpha} = \alpha \tag{A16}$$

where $\hat{\alpha}$ is the vertical scaling factor in the spatial domain. Therefore, the amplitude factor α derived from spectral analysis can be directly used to compare purely vertical scaling in the spatial domain.

Appendix B: The Transition From Wave Propagation to Diffusion in Fluid Dynamics

In this section we consider the simplest model of one-dimensional propagation of gravity-driven waves at the surface of a fluid layer. We assume a layer of constant thickness on a horizontal plane in shallow-water

approximation, which means that flow is only horizontal and constant over depth, pressure is hydrostatic, and acceleration is due to pressure differences arising from the topography of the fluid surface. If $u(x,t)$ is the height of the fluid surface above the undisturbed surface and $v(x,t)$ the horizontal velocity, the acceleration is

$$\frac{\partial}{\partial t}v(x,t) = -\frac{\partial}{\partial x}u(x,t) - \eta v(x,t). \tag{B1}$$

The first term at the right-hand side describes acceleration by pressure gradients, while the second term introduces viscous friction. All physical parameters (density, gravity, undisturbed thickness) have been omitted for simplicity except for the parameter of friction η (which is related to the viscosity of the fluid). The nonlinear part of the acceleration term has also been neglected here, which means that the velocity has to be small. The second equation required for closure of the system describes the conservation of mass. In linearized form (corresponding to a small amplitude $u(x,t)$), it reads

$$\frac{\partial}{\partial t}u(x,t) = -\frac{\partial}{\partial x}v(x,t). \tag{B2}$$

Let us now consider harmonic oscillations in topography and velocity according to

$$u(x,t) = f(t)e^{ikx} \tag{B3}$$

$$v(x,t) = g(t)e^{ikx} \tag{B4}$$

Then equations (B1) and (B2) lead to the system of ordinary differential equations

$$\frac{d}{dt}\begin{pmatrix} f(t) \\ g(t) \end{pmatrix} = \begin{pmatrix} 0 & -ik \\ -ik & -\eta \end{pmatrix}\begin{pmatrix} f(t) \\ g(t) \end{pmatrix}. \tag{B5}$$

The fundamental solutions of this system are of the form $e^{\lambda t}$ where

$$\lambda = -\frac{\eta}{2} \pm \sqrt{\left(\frac{\eta}{2}\right)^2 - k^2} \tag{B6}$$

are the eigenvalues of the 2×2 matrix. Both eigenvalues are complex with negative real parts if $\eta < 2k$. This solution describes the propagation of waves where the amplitude decreases through time. In turn, both eigenvalues are real and negative for strong friction, that is, for $\eta \geq 2k$. Then wave propagation ceases, and the pattern only decays through time. These results imply that the simplest model for viscous flow turns from wave propagation at low friction into a diffusion-type behavior at high friction.

Acknowledgments
The image data that support the findings of this study are available in the Planetary Data System at https://pds-imaging.jpl.nasa.gov/volumes/mro.html (License: U.S. Government Works). Derived data sets and code for this research are available in these in-text data citation references: Pietrek et al. (2019), [License: CC-BY 4.0]. The constructive comments of S. M. Baloga and an anonymous referee are greatly appreciated. This work was funded by the DFG Grant KE 732/19-3 and a scholarship grant of the LGFG Baden-Württemberg.

References

Aharonson, O., Zuber, M., & Rothman, D. H. (2001). Statistics of Mars' topography from Mars Orbiter Laser Altimeter: Slopes, correlations, and physical models. *Journal of Geophysical Research: Planets*, *106*, 23,723–23,735. https://doi.org/10.1029/2000JE001403

Balmino, G. (1993). The spectra of topography of Earth, Venus and Mars. *Geophysical Research Letters*, *20*, 1063–1066. https://doi.org/10.1029/93GL01214

Barlow, N. G. (2005). A review of Martian impact crater ejecta structures and their implications for target properties. *Large Meteorite Impacts III*, *384*, 433–442. https://doi.org/10.1130/0-8137-2384-1.433

Barlow, N. G., Boyce, J. M., Costard, F. M., Craddock, R. A., Garvin, J. B., Sakimoto, S. E. H., et al. (2000). Standardizing the nomenclature of Martian impact crater ejecta morphologies. *Journal of Geophysical Research*, *105*, 26,733–26,738. https://doi.org/10.1029/2000JE001258

Barnouin-Jha, O. S., Baloga, S., & Glaze, L. (2005). Comparing landslides to fluidized crater ejecta on Mars. *Journal of Geophysical Research*, *110*, E04010. https://doi.org/10.1029/2003JE002214

Belousov, A., Belousova, M., & Voight, B. (1999). Multiple edifice failures, debris avalanches and associated eruptions in the Holocene history of Shiveluch volcano, Kamchatka, Russia. *Bulletin of Volcanology*, *61*, 324–342. https://doi.org/10.1007/s004450050300

Boyce, J. M., & Mouginis-Mark, P. J. (2006). Martian craters viewed by the thermal emission imaging system instrument: Double-layered ejecta craters. *Journal of Geophysical Research*, *111*, E10005. https://doi.org/10.1029/2005JE002638

Carr, M. H., Crumpler, L. S., Cutts, J. A., Greeley, R., Guest, J. E., & Masursky, H. (1977). Martian impact craters and emplacement of ejecta by surface flow. *Journal of Geophysical Research*, *82*(28), 4055–4065. https://doi.org/10.1029/JS082i028p04055

DeBlasio, F. V. (2011). Landslides in Valles Marineris (Mars): A possible role of basal lubrication by sub-surface ice. *Planetary and Space Science*, *59*, 1384–1392. https://doi.org/10.1016/j.pss.2011.04.015

Dufresne, A., & Davies, T. R. (2009). Longitudinal ridges in mass movement deposits. *Geomorphology*, *105*, 171–181. https://doi.org/10.1016/j.geomorph.2008.09.009

Forterre, Y., & Pouliquen, O. (2001). Longitudinal vortices in granular flows. *Physical Review Letters*, *86*(26), 5886–5889. https://doi.org/10.1103/PhysRevLett.86.5886

Fox, C. G., & Hayes, D. E. (1985). Quantitative methods for analysing the roughness of the seafloor. *Reviews of Geophysics*, *23*, 1–48.

Hergarten, S. (2002). *Self-organized criticality in Earth systems*. Berlin, Heidelberg, New York: Springer.

Johnson, B. (1978). Blackhawk landslide, California, U.S.A. In B. Voight (Ed.), *Rockslides and avalanches* (pp. 257–361). Amsterdam: Elsevier.

Komatsu, G., Ori, G. G., Lorenzo, S. Di, Rossi, A. P., & Neukum, G. (2007). Combinations of processes responsible for Martian impact crater layered ejecta structures emplacement. *Journal of Geophysical Research*, *112*, E06005. https://doi.org/10.1029/2006JE002787

Lagain, A., Bouley, S., & Costard, F. (2015). Datation of multiple-layer ejecta crater on Mars. In *In 46th lunar and planetary science conference*, pp. #1920.

Little, S. A., Carter, P. H., & Smith, D. K. (1993). Wavelet analysis of a bathymetric profile reveals anomalous crust. *Geophysical Research letters*, *20*, 1915–1918.

Lucchitta, B. K. (1979). Landslides in Valles Marineris, Mars. *Journal of Geophysical Research*, *84*, 8097–8113. https://doi.org/10.1029/JB084iB14p08097

Magnarini, G., Mitchell, T. M., Grindrod, P. M., Goren, L., & Schmitt, H. H. (2019). Longitudinal ridges imparted by high-speed granular flow mechanisms in Martian landslides. *Nature Communications*, *10*, 4711. https://doi.org/10.1038/s41467-019-12734-0

Malamud, B. D., & Turcotte, D. L. (2001). Wavelet analysis of Mars polar topography. *Journal of Geophysical Research*, *106*, 17,497–17,504. https://doi.org/10.1029/2000JE001333

Malin, M. C., Bell, J. F., Cantor, B. A., Caplinger, M. A., Calvin, W. M., Clancy, R. T., et al. (2007). Context camera investigation on board the Mars Reconnaissance Orbiter. *Journal of Geophysical Research*, *112*, E05S04. https://doi.org/10.1029/2006JE002808

Mandelbrot, B. (1967). How long is the coast of Britain? Statistical self-similarity and fractional dimension. *Science*, *156*, 636–638.

Mazzanti, P., DeBlasio, F. V., DiBastiano, C., & Bozzano, F. (2016). Inferring the high velocity of landslides in Valles Marineris on Mars from morphological analysis. *Earth, Planets and Space*, *68*, 636–638. https://doi.org/10.1186/s40623-015-0369-x

McEwen, A. S., Eliason, E. M., Bergstrom, J. W., Bridges, N. T., Hansen, C. J., Delamere, W. A., et al. (2007). Mars Reconnaissance Orbiter's High Resolution Imaging Science Experiment (HiRISE). *Journal of Geophysical Research: Planets*, *112*, E05S02. https://doi.org/10.1029/2005JE002605

McSaveney, M. J. (1987). Sherman glacier rock avalanche, Alaska, U.S.A. In B. Voight (Ed.), *Rockslides and avalanches* (pp. 197–258). Amsterdam: Elsevier.

Moratto, Z. M., Broxton, M. J., Beyer, R. A., Lundy, M., & Husmann, K. (2010). Ames Stereo Pipeline, NASA's open source automated stereogrammetry software. In *41th lunar and planetary science conference*, pp. #2364.

NASA (2017). The Ames Stereo Pipeline: NASA's open source Automated Stereogrammetry Software. a part of the NASA Neo Geography Toolkit version 2.6.0. NASA Ames Research Center.

Naranjo, J. A., & Francis, P. (1987). High velocity debris avalanche at Lastarria Volcano in the North Chilean Andes. *Bulletin of Volcanology*, *49*, 509–514. https://doi.org/10.1007/BF01245476

Nikora, V., & Goring, D. (2004). Mars topography: Bulk statistics and spectral scaling. *Chaos, Solitons and Fractals*, *19*, 427–439. https://doi.org/10.1016/S0960-0779(03)00054-7

Nikora, V., & Goring, D. (2006). Spectral scaling in Mars topography: Effect of craters. *Acta Geophysica*, *54*, 102–112. https://doi.org/10.2478/s11600-006-0009-8

Oberbeck, V. R. (1975). The role of ballistic erosion and sedimentation in lunar stratigraphy. *Reviews of Geophysics*, *13*, 337–362. https://doi.org/10.1029/RG013i002p00337

Osinski, G. R. (2006). Effect of volatiles and target lithology on the generation and emplacement of impact crater fill and ejecta deposits on Mars. *Meteoritics and Planetary Science*, *41*, 1571–1586. https://doi.org/10.1111/j.1945-5100.2006.tb00436.x

Pelletier, J. D., & Turcotte, D. L. (1996). Scale-invariant topography and porosity variations in fluvial sedimentary basins. *Journal of Geophysical Research*, *101*, 28,165–28,175. https://doi.org/10.1029/96JB02848

Pietrek, A., Hergarten, S., & Kenkmann, T. (2019). Supporting information for "Morphometric characterization of longitudinal striae on Martian landslides and impact ejecta blankets and implications for the formation mechanism". https://osf.io/q7jb2/.OSF

Pouliquen, O., & Vallance, J. W. (1999). Segregation induced instabilities of granular fronts. *Chaos*, *9*(3), 621–630. https://doi.org/10.1063/1.166435

Quantin, C., Allemand, P., & Delacourt, C. (2004). Morphology and geometry of Valles Marineris landslides. *Planetary and Space Science*, *52*, 1011–1022. https://doi.org/10.1016/j.pss.2004.07.016

Robbins, S. J., & Hynek, B. M. (2012). A new global database of Mars impact craters $\geq$ 1 km: 1. Database creation, properties, and parameters. *Journal of Geophysical Research*, *117*, E05004. https://doi.org/10.1029/2011JE003966

Schultz, P. H. (1992). Atmospheric effects on Martian ejecta emplacement. *Journal of Geophysical Research*, *92*, 11,623–11,662. https://doi.org/10.1029/92JE00613

Schultz, P. H., & Gault, D. E. (1979). Atmospheric effects on ejecta emplacement. *Journal of Geophysical Research*, *84*, 7669–7687. https://doi.org/10.1029/JB084iB13p07669

Shaller, P. J. (1991). Analysis and implications of large martian and terrestrial landslides (Ph.D. Thesis), California Institute of Technology.

Shreve, R. L. (1966). Sherman landslide, Alaska. *Science*, *154*, 1639–1643. https://doi.org/10.1126/science.154.3757.1639

Smith, P. C. (1973). A similarity solution for slow viscous flow down an inclined plane. *Journal of Fluid Mechanics*, *58*, 275–288. https://doi.org/10.1017/S0022112073002594

Tanaka, K. L., Robbins, S. J., Fortezzo, C. M., Skinner jr, J. A., & Hare, T. M. (2014). The digital global geologic map of Mars: Chronostratigraphic ages, topographic and crater morphologic characteristics, and updated resurfacing history. *Planetary and Space Science*, *95*, 11–24. https://doi.org/10.1016/j.pss.2013.03.006

Turcotte, D. L. (1987). A fractal interpretation of topography and geoid spectra on the Earth, Moon, Venus, and Mars. *Journal of Geophysical Research*, *92*(B4), E597–E601.

Turcotte, D. L., & Schubert, G. (1982). *Geodynamics*. New York, Chichester, Brisbane: Wiley & Sons.

Valderrama, P., Roche, O., Samaniego, P., van Wyk de Vries, B., Bernard, K., & Marino, J. (2016). Dynamic implications of ridges on a debris avalanche deposit at Tutupaca volcano (southern Peru). *Bulletin of Volcanology*, *78*, 14. https://doi.org/10.1007/s00445-016-1011-x

Weiss, D. K., & Head, J. W. (2013). Formation of double-layered ejecta craters on Mars: A glacial substrate model. *Geophysical Research Letters*, *40*, 3819–3824. https://doi.org/10.1002/grl.50778

Weiss, D. K., & Head, J. W. (2014). Ejecta mobility of layered ejecta craters on Mars: Assessing the influence of snow and ice deposits. *Icarus*, *233*, 131–146. https://doi.org/10.1016/j.icarus.2014.01.038

Wulf, G., & Kenkmann, T. (2015). High-resolution studies of double-layered ejecta craters: Morphology, inherent structure, and a phenomenological formation model. *Meteoritics and Planetary Science*, *50*, 173–203. https://doi.org/10.1111/maps.12416